ACS Energy LETTERS

http://pubs.acs.org/journal/aelccp

Self-Photocatalytic Splitting of Carbon Dioxide Using Co-cationic Perovskite Nanocrystals in the Absence of Water

Sumit S. Bhosale,[#] Aparna K. Kharade,[#] Sudhakar Narra, Sue-min Chang,* and Eric Wei-Guang Diau*

Cite This: *ACS Energy Lett.* 2023, 8, 280−288

Read Online

ACCESS | Metrics & More | Article Recommendations | Supporting Information

ABSTRACT: Environmental concerns demand efficient removal of CO_2, a major greenhouse gas. For this purpose, a traditional chemical strategy implements a catalytic conversion of CO_2 to CO, with H_2O as the sacrificial agent to generate O_2. Herein we report the first self-photocatalytic conversion of CO_2 to generate CO and O_2 in the absence of H_2O, using co-cationic perovskite nanocrystal $Cs_{0.55}FA_{0.45}PbBr_3$. We obtained a record production rate 105 μmol g^{-1} h^{-1} of CO, which is three times that with $CsPbBr_3$ as photocatalyst at the gas−solid interface. During photocatalytic reaction, a phase transition occurred with an enlarged crystal size through the effect of Ostwald ripening, for which the CO yield approached 3.1 mmol g^{-1} within the reaction period of ∼60 h. During this process, both FA and oleylammonium cations were released to provide the proton source for the CO_2 reduction to proceed and generate hydroxyl species required for oxidation. A self-photocatalysis mechanism involving bound hydroxyls is proposed.

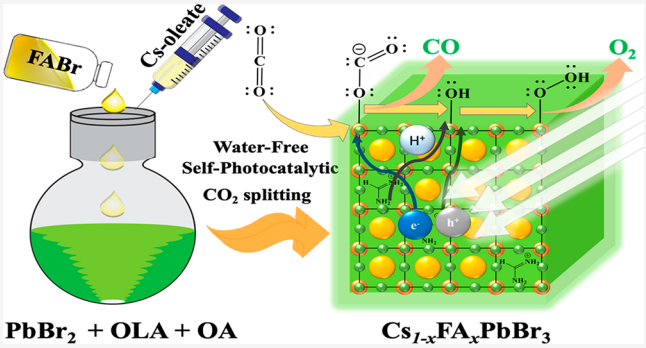

Greenhouse gases are responsible for climate change, which includes melting of polar ice, rising sea levels, raging fires and diminished biodiversity. Carbon dioxide, the most important greenhouse gas, is rapidly increasing as a result of various human activities, with the burning of fossil fuels for energy being a major crisis in the world. One promising solution of these problems is to convert CO_2 into valuable fuels through artificial photosynthesis. Natural photosynthesis is an almost perfect reaction in the world, evolving over millions of years, but its replication is difficult. Global researchers have nonetheless proposed various semiconductor materials to implement photocatalytic reduction of CO_2.[1−3] Because of their defect-tolerant nature, perovskite nanocrystals (PeNCs) have excellent optical properties; their syntheses are feasible. For photocatalytic reduction of CO_2, both all-inorganic and organic−inorganic PeNCs are reported.[4,5] Due to its effective optical characteristics, stability, and appropriate energy levels, $CsPbBr_3$ PeNC has served extensively for photocatalytic applications.[6] Xu et al.[4] first reported CO_2 reduction by $CsPbBr_3$ PeNC; several studies on $CsPbBr_3$ PeNC have since improved the catalytic yields, such as with ligand modification,[7] heterojunction formation,[8,9] B-site doping,[10] and halide mixing;[11] the best reported CO-production rate is 45 μmol g^{-1} h^{-1} based on $Cs_3Bi_2Br_9$ perovskite quantum-dot photocatalyst at the gas−solid interface.[12] Recently, many authors reported greater rates of CO production based on experiments performed in liquid media,[6,13] in which the CO yields might be overestimated because of photodecomposition of the solvent such as ethyl acetate or due to photocatalytic organic transformation involving the organic solvent and oxygen.[14−16] The reaction medium is a critical issue for CO_2 reduction; because perovskite is sensitive to moisture, water and polar solvents cannot serve to dissolve CO_2. We previously[14] conducted photocatalytic CO_2 reduction in a gas−solid system in which CO_2 gas bubbled through water saturated the surface of PeNC with H_2O and CO_2. Water oxidation is an important counter-reaction to provide extra protons for CO_2 reduction, but small amounts of water inside PeNC influence the crystallinity of perovskite and degrade the nanocrystals to some extent, preventing attainment of the best catalytic performance. Because the yields of CO generated with PeNC photocatalysts are degraded by moisture, we here report for the first time

Received: October 16, 2022
Accepted: November 23, 2022

https://doi.org/10.1021/acsenergylett.2c02342
ACS Energy Lett. 2023, 8, 280−288

photocatalytic splitting of CO_2 using a co-cationic PeNC as an efficient catalyst without water. The CO production rate attained 105 μmol g^{-1} h^{-1}, which is three times that using $CsPbBr_3$ PeNC as a catalyst at the gas−solid interface. This CO production rate is also more than 2.3 times the previous record reported elsewhere.[12] We discovered that CO_2 was involved in both reduction and oxidation channels—a process of self-photocatalysis to split CO_2 into CO and O_2 that has not been achieved previously.

According to a schematic demonstration in Figure 1, mixed cationic PeNC, $Cs_{1-x}FA_xPbBr_3$ (abbreviated as CF; FA

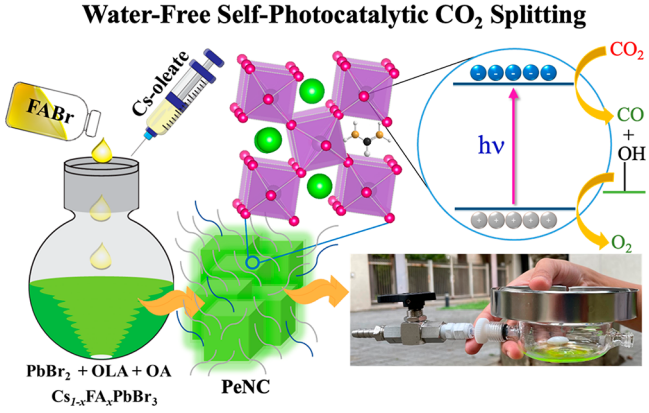

Figure 1. Schematic representation showing synthesis of perovskite nanocrystals (PeNCs) and photocatalytic splitting of CO_2. Abbreviations FABr, OA, and OLA indicate formamidinium bromide, oleic acid, and oleylamine, respectively. The waves on PeNCs represent the attached surface ligands OA and OLA. The photographic image shows our actual moisture-free reactor.

represents formamidinium), were synthesized using the hot addition method.[17,18] $CsPbBr_3$ (abbreviated CS hereafter) PeNC was also synthesized through the traditional hot injection method for comparison.[19] The co-cation FA inside CF PeNC had an effect to tune the electronic properties and to improve the stability of PeNC.[17] We used dry CO_2 instead of moist CO_2 to adsorb on the surface of PeNC fully covered with organic ligands such as oleic acid (OA, major part) and oleylamine (OLA, minor part) in their ionic forms.

The morphological features of the synthesized CS and CF PeNCs are viewed in the TEM images shown in Figure 2a,b, respectively; both PeNCs have cubic unit cells and are highly crystalline with average nanocrystal size ∼8 nm. XRD patterns of CS and CF shown in Figure 2c,d are broad enough for the PeNC to include both cubic and orthorhombic crystal phases. Total pattern solution (TOPAS) analysis was performed to identify the crystal phases for these PeNCs.[20]Figure S1 shows the results of TOPAS fits for both PeNC samples, with the fit parameters listed in Table S1. Based on TOPAS fits, both PeNCs have mixed cubic and orthorhombic phases of varied proportions. CF comprises of 7% cubic and 93% orthorhombic phases; CS has 38% cubic and 62% orthorhombic phases. The orthorhombic phase has a much larger unit cell than the cubic phase (Table S1), implying that CF might have more space than CS to adsorb CO_2 molecules on the crystal surface to enhance its photocatalytic performance. The CS PeNC exhibits a small signal at $2\theta \sim 12.3°$ due to formation of a zero-dimensional Cs_4PbBr_6 perovskite phase,[21] but for CF PeNC such an impurity phase is insignificant. The interplanar distance determined with TEM analysis indicates that lattice spacing 0.291 nm for CS belongs to cubic crystal plane (002) or orthorhombic crystal plane (040). Similarly, lattice spacing of 0.285 nm for CF belongs to cubic crystal plane (002) or orthorhombic crystal plane (212), both according to a TOPAS analysis.

We performed XRD measurements after photocatalytic CO_2 reduction to test the stability of PeNCs in the presence of CO_2 after irradiation for 12 h (Figure 2c,d). These results show that the diffraction signals become sharper after CO_2 reduction, indicating an increased crystal size as a result of removal of surface ligands, a phenomenon similar to the effect of Ostwald ripening in solution samples.[22] The TOPAS fit of XRD after CO_2 reduction shows a cubic phase enhanced from 38% to 73% for CS and from 7% to 47% for CF (Table S1). The aggregation and enhanced crystal size due to light-induced ligand removal in CF PeNC are directly observed in TEM images shown in Figure S2. By checking the color change of the sample before and after the photocatalytic reaction, it is possible to conclude the change in crystal size upon light irradiation. Figure S3 shows the photo images of the reactor before (green) and after CO_2 reduction for 60 h (yellow). According to the CF absorption spectra shown in Figure S4, after CO_2 reduction for 12 h, the band edge absorption exhibits bathochromic shift, which is consistent with the growth of the crystal size upon irradiation. Figure S5 panels a and b show the TEM-EDX and SEM-EDX analysis results, respectively. Because the TEM images were obtained by a much greater electron energy than SEM, the sample might be damaged via TEM-EDX measurements with prolonged exposure to the electron beams. Therefore, the composition of $Cs_{1-x}FA_xPbBr_3$ PeNC was determined using the SEM-EDX technique at three different areas, as shown in Figure S5b. The TEM image is a transmission type, so its EDX analysis determines the composition of the CF structure in the bulk state. In contrast, for the SEM image it is a reflective type (secondary electrons) so its EDX determines mostly the chemical structure on the surface of CF. For the SEM-EDX results, first, we found that all three SEM areas show a Br/Pb ratio to be ∼3.5, indicating that the surface of CF is bromide rich, which helps on coordination of Br to OLA to provide an extra proton source for CO_2 reduction. Second, the x value in $Cs_{1-x}FA_xPbBr_3$ can be determined by assigning the stoichiometric ratio of Pb/(Cs+FA) to be 1. Based on averaging of three sets of the SEM-EDX data shown in Figure S5b, we conclude that the proportions of Pb and Cs are 20% and 11%, respectively. Therefore, we obtained the fraction of FA to be x = 0.45 so that CF can be determined with the formulas $Cs_{0.55}FA_{0.45}PbBr_3$. 45% of FA on the surface of CF should have the effect to provide more protons for CO_2 reduction to proceed.

We also investigated the optical properties and carrier relaxation dynamics of both PeNCs for the pristine film in a dark, pristine film photoactivated for 12 h and CO_2 adsorbed film photoactivated for 12 h, as the results reported elsewhere.[23] We found that photoactivation significantly enhances the possibility of charge separation and retards the charge recombination so that these photogenerated charge carriers would have more chances to participate in the following catalytic reaction. The comparison between CS and CF samples shows that the CF samples had slower charge recombination than the CS samples for all cases, indicating that the CF sample is more suitable than the CS sample for photocatalytic experiments.[23]

https://doi.org/10.1021/acsenergylett.2c02342
ACS Energy Lett. 2023, 8, 280−288

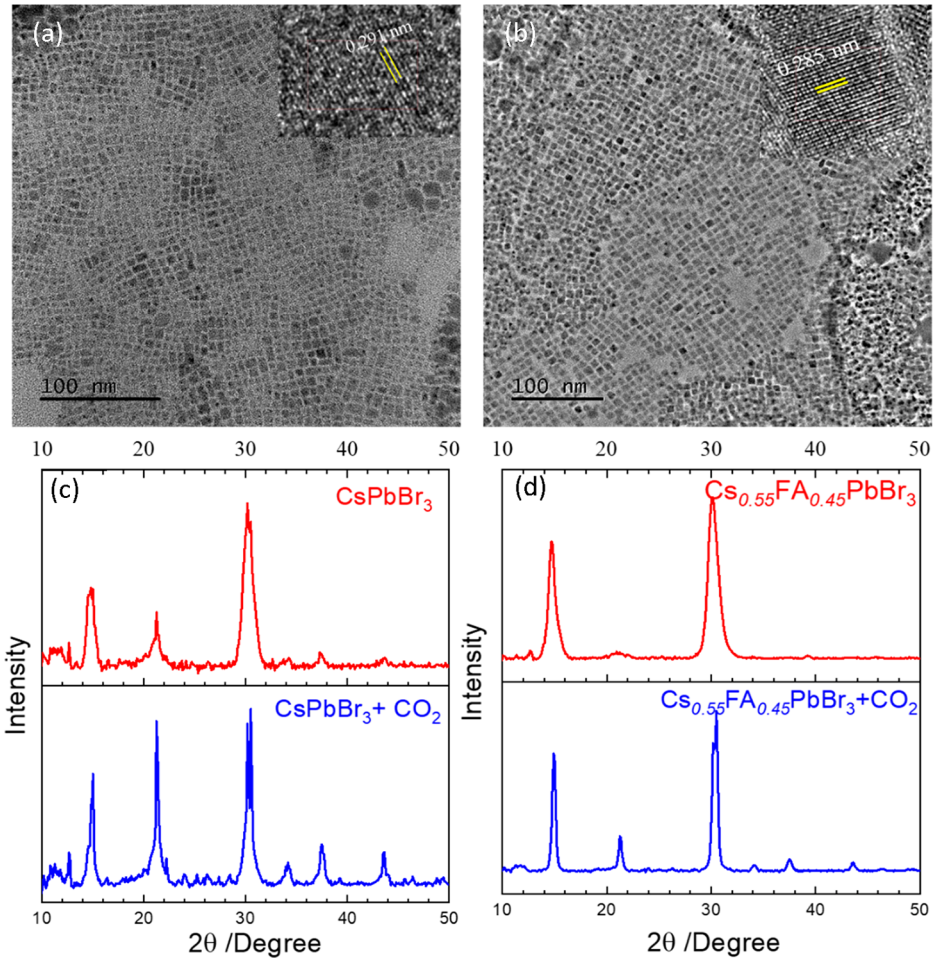

Figure 2. Transmission electron-microscope (TEM) images and X-ray diffraction (XRD) patterns of PeNC films. (a) TEM of $CsPbBr_3$. (b) TEM of $Cs_{0.55}FA_{0.45}PbBr_3$. (c) XRD of $CsPbBr_3$. (d) XRD of $Cs_{0.55}FA_{0.45}PbBr_3$. The red and blue traces in (c) and (d) were recorded before and after one sun irradiation for 12 h in the presence of CO_2, respectively.

To implement photocatalytic CO_2 reduction for CS and CF PeNCs, we used a reaction setup similar to that previously reported.[14] First, we dispersed PeNC in toluene solution (~0.3 mL) and evenly dropped the solution at the bottom of the reactor. Second, we manually rotated the reactor to form a uniform PeNC suspension inside the reactor. Third, we completely evaporated the toluene solvent and then passed a nitrogen flow to the reactor for 30 min to remove oxygen and residual toluene. Care must be taken to remove residual solvents as they might produce unexpected products as reported elsewhere.[15,16] Figure S6 displays the GC-FID analysis results, which confirm that there was no residual toluene left in the reactor. Figure 3a shows the average yields of products CO and O_2 for both CS and CF catalysts after 1 sun irradiation for 12 h, for which CF produced CO 1.11 ± 0.08 and O_2 0.61 ± 0.12 mmol g^{-1} (Table S2); in contrast, CS produced CO 0.35 ± 0.04 and O_2 0.19 mmol g^{-1}. We summarize all product yields in Table S2 for which a record rate of CO production, with the best value of 105 μmol g^{-1} h^{-1} and an average value of 92 μmol g^{-1} h^{-1} obtained without water, which is more than twice the previous record[12] in the presence of water.

The CO yield of CF was three times that of CS, which might arise for three reasons. First, CF has a proportion of the orthorhombic phase much greater than that of CS, which might provide more vacancies for CO_2 adsorption. Second, the hot-addition method produced a surface richer in halide (as also shown by the SEM-EDX results) than the traditional hot-injection method,[17] indicating that the oleylammonium ion is more abundant on the surface of CF than on CS to attach to the bromide ligand, so that more protons can be supplied for CF than for CS. Third, CF also contains a FA cation serving as a base on the surface, which might attract an acidic CO_2 molecule and provide an additional proton source for CO_2 reduction. Note that after irradiation, the crystal size increases, but the size of the unit cell decreases due to phase transition from orthorhombic to cubic. For CF, it means that more FA can be released upon photoreduction to proceed, and these FA cations can release more protons to help CO_2 reduction so as to attain higher CO production yields than the CS sample. The product yields of O_2 are approximately half those of CO, consistent with this overall reaction of CO_2 to generate CO and O_2 in a self-catalysis reaction:

$$CO_2 \rightarrow CO + \frac{1}{2}O_2 \quad (1)$$

In the presence of water, the half reactions of CO_2 reduction and H_2O oxidation are expressed as

$$CO_2 + 2H^+ + 2e^- \rightarrow CO + H_2O \qquad E^0_{red} = -0.106\ V \quad (2)$$

https://doi.org/10.1021/acsenergylett.2c02342
ACS Energy Lett. 2023, 8, 280−288

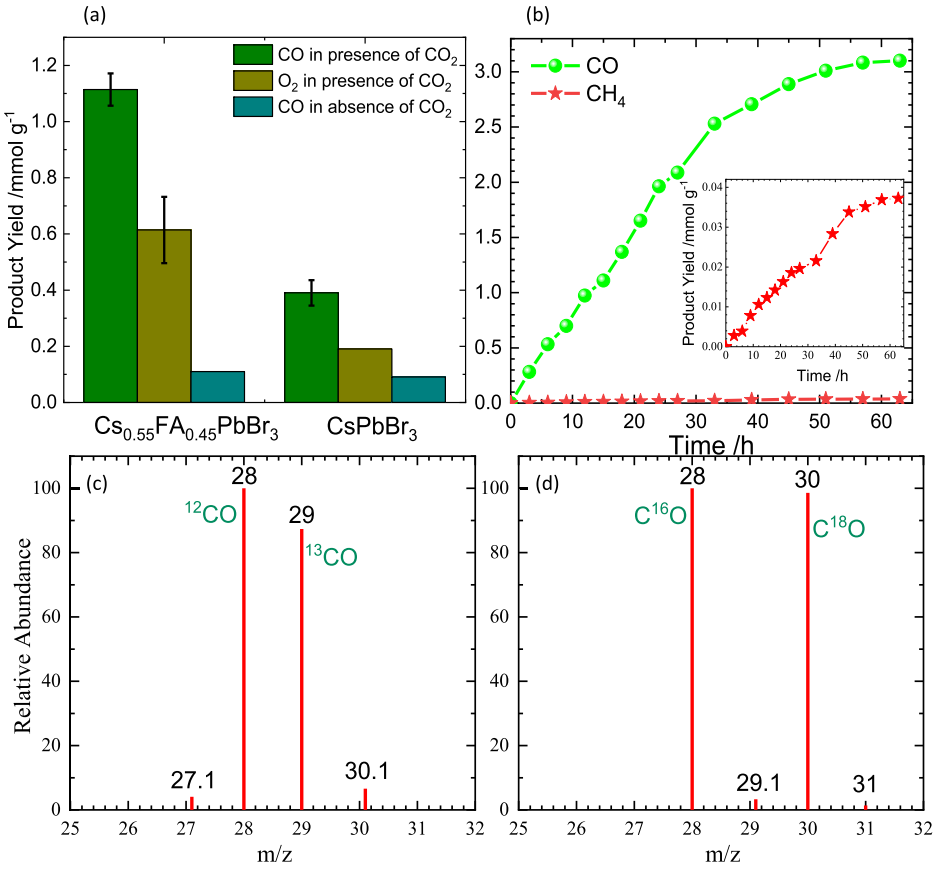

Figure 3. Yields of CO and O_2 and temporal evolution of CO. (a) Yields of CO and O_2 in the presence of CO_2 and of CO in the absence of CO_2 after photocatalytic reactions of $Cs_{0.55}FA_{0.45}PbBr_3$ and $CsPbBr_3$ PeNC for 12 h. (b) Yields of CO as a function of duration of irradiation for $Cs_{0.55}FA_{0.45}PbBr_3$ PeNC with yields of CH_4 shown in the inset. (c) and (d) show the isotopic GC−MS data after photocatalytic reduction of $^{13}CO_2$ and photocatalytic reduction of $C^{18}O_2$, respectively. For (c) and (d), the isotopic gases were purged for less than 2 min, and the reaction period was 12 h (GC−MS raw data are presented in Figure S11). All the photocatalytic reactions were carried out under one sun irradiation using a calibrated solar simulator.

$$H_2O \rightarrow \frac{1}{2}O_2 + 2H^+ + 2e^- \qquad E^0_{ox} = -1.229\ V \tag{3}$$

(see refs 24 and 25, respectively) to attain the total redox potential −1.335 V for reaction 1. We performed experiments also with CO_2 bubbled through water; the corresponding yields of CO and methane for both CF and CS are shown in Figure S7 with the results listed in Table S2. These yields of CO are only half that for CF in the presence of water relative to the absence of water but are similar for CS in the presence or absence of water. Furthermore, in the presence of water, the CO yield for CF was only twice that for CS because some active sites of PeNCs were occupied by water so that oxidation through reaction 3 became a bottleneck for reaction 1 to proceed. Reactions 2 and 3 are unsuitable to interpret our data obtained in the absence of water, which will be discussed in the later section regarding the reaction mechanism of the Supporting Information.

The CO_2 reduction using CF PeNC as a catalyst was traced every 3 h. As shown in Figure 3b, formation of CO increases linearly until irradiation for ∼30 h. Thereafter, the increase in CO production slowed and approached an asymptotic point at an irradiation duration over 60 h, at productions of CO and methane of 3.1 and 0.037 mmol g^{-1}, respectively. To our best knowledge, no report of a total yield of CO production attained such a high level (>3 mmol g^{-1}) with an irradiation period extended over 60 h, in particular, for experiments carried out at the gas−solid interface. The stability and recycling ability of the CF photocatalyst were performed by repeating the reaction every 12 h for 6 runs; for each run, we made a GC analysis, pumped out the gases from the reactor, and refilled with fresh CO_2 for the next run. Figure S8 displays the results, which demonstrate a progressive decline in product yields for each run as a consequence of an increase in the size of perovskite nanocrystals and a change in their crystal structure as a result of the loss of oleylammonium and formamidinium throughout the reduction process. The involvement of the ammonium cation in the reduction process is explained in the later section discussing the recation mechanism of the Supporting Information.

As control experiments, we irradiated both PeNC samples in a sealed reactor with N_2 rather than CO_2 for 12 h; the CO yields were 0.115 mmol g^{-1} for CF and 0.092 mmol g^{-1} for CS. As nearly the same amount of CO was produced in these control experiments, we concluded that CO was formed through redox reaction of the ligands because both PeNC samples had the same surface ligands. For the CF sample the CO yield in the presence of CO_2 was ten times that without CO_2 (Figure S9), which proves that CO was produced mostly by reduction of CO_2. For confirmation, we undertook an isotopic experiment with $^{13}CO_2$ gas passing through the reactor under the vacuum conditions (Experimental Procedure); the corresponding GC−MS results in Figure S10 and

https://doi.org/10.1021/acsenergylett.2c02342
ACS Energy Lett. 2023, 8, 280−288

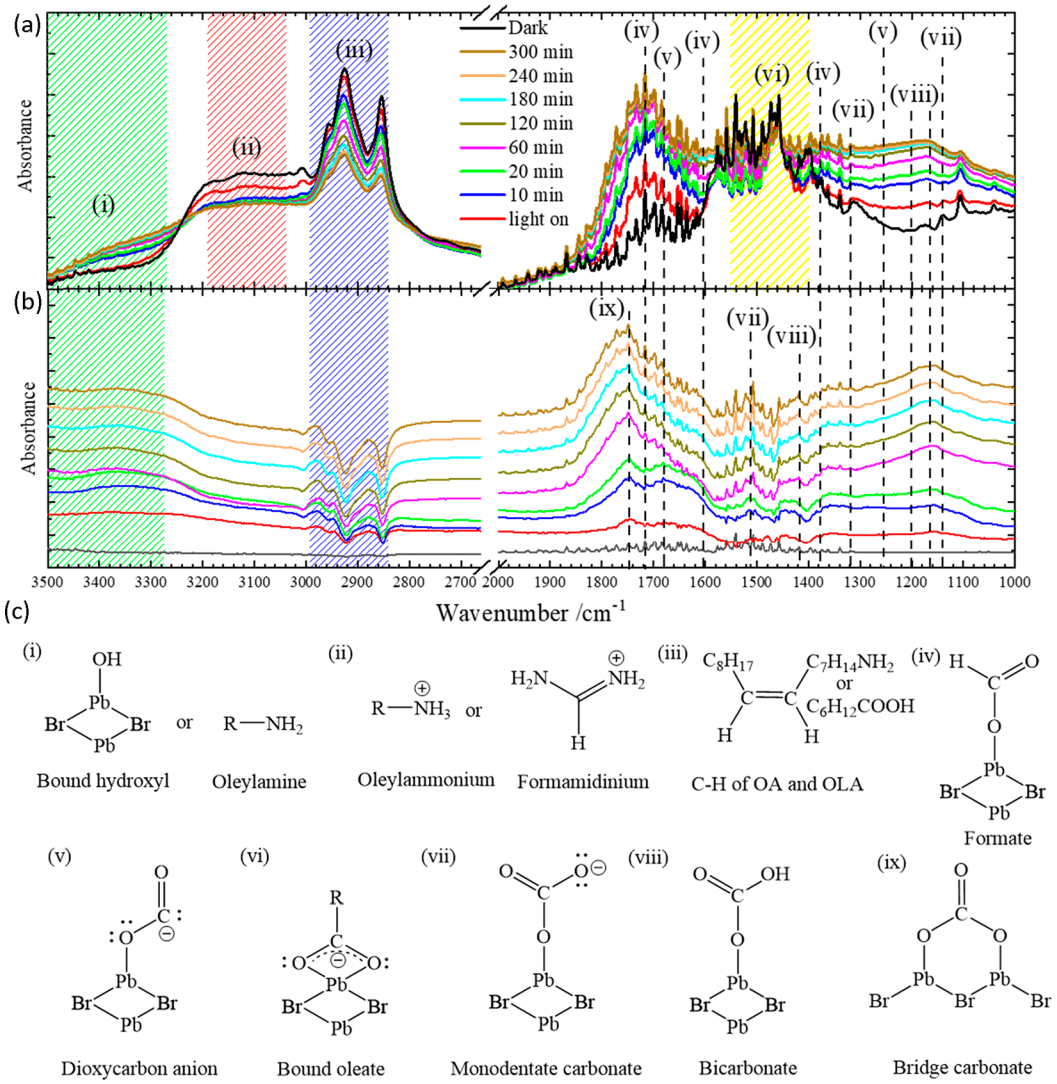

Figure 4. Diffuse-reflectance mid-infrared spectra of $Cs_{0.55}FA_{0.45}PbBr_3$ in the presence of CO_2 and species involved. (a) Recorded from blank KBr as reference. (b) Recorded from CF PeNC/N_2 as reference. A set of spectra was collected in each case under illumination for varied periods as indicated. (c) Chemical species labeled in (a) and (b) with assignments according to literature reports (refer to Table S3). R in (i), (ii), and (vi) represents the oleyl species.

Figure 3c show mass spectra from $^{12}CO_2$ and $^{13}CO_2$ reduction reactions, respectively. The isotopic abundance of CO 29 m/z was large in $^{13}CO_2$ reduction (the intensity of CO 28 m/z is still large because of a redox reaction of surface ligands and short duration of $^{13}CO_2$ loading which is less than 2 min) but was scarcely observed in $^{12}CO_2$ reduction, confirming the production of CO from CO_2.

Study of the oxidation pathway together with the reduction pathway is crucial because it provides the electron and proton sources needed for the reduction process to proceed. We therefore performed the isotopic experiments with $C^{18}O_2$ gas in order to determine whether the source of oxygen came from the photocatalytic reaction of CO_2. Figure 3d depicts the formation of CO from the isotopic gases showing both the 28 m/z and 30 m/z peaks with similar abundance, confirming that the source of CO is coming from CO_2 reduction, similar to the result obtained from the $^{13}CO_2$ experiment. On the other hand, a significant amount of adventitious oxygen that was entering the GC−MS system during the injection procedure and this gave a tiny amount of isotopic oxygen at mass 36 m/z. Under such a condition, we chose to compare the mass ratio of 36 m/z ($^{18}O_2$) with respect to 32 m/z ($^{16}O_2$) between the blank and the $C^{18}O_2$ isotopic reaction. For the blank condition, only pure CO_2 gas was injected to the GC−MS system; for the isotopic reaction, photocatalytic $C^{18}O_2$ reactions were performed for 12 h and then the gas sample was injected to the GC−MS system. The results of blank and isotopic reactions are shown in Figure S12. It is apparent that the $^{18}O_2/^{16}O_2$ mass ratio of the isotopic reaction was 1 order of magnitude greater than that of the blank, confirming the concept of self-photocatalysis for the oxygen to be generated from splitting of CO_2 in the absence of water, and the corresponding mechanism will be discussed in what follows.

To investigate the paths of photocatalytic oxidation and reduction for conversion of CO_2 to CO and O_2 in the absence of water, we recorded diffuse-reflectance infrared Fourier-transform (DRIFT) spectra in situ. Figure 4a shows these spectra of CF using blank KBr as the reference; Figure 4b shows DRIFT spectra of CF with PeNC/N_2 as reference; Figure 4c shows plausible assignments for chemical species in these spectra with precise spectral assignments in Table S3.

https://doi.org/10.1021/acsenergylett.2c02342
ACS Energy Lett. 2023, 8, 280−288

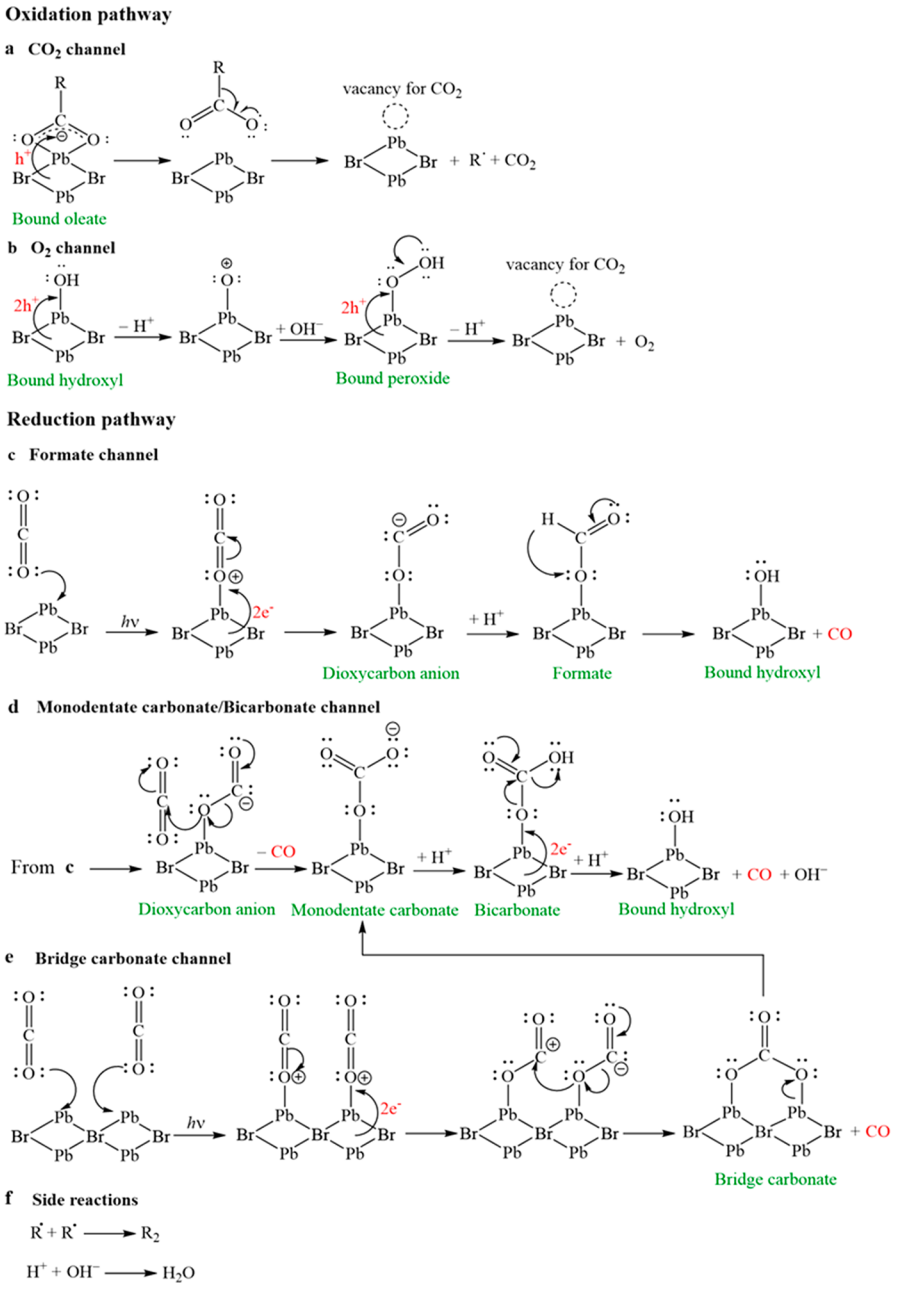

Figure 5. Plausible mechanism for oxidation, reduction, and side channels of photocatalytic conversion of CO_2 with $Cs_{0.55}FA_{0.45}PbBr_3$ as photocatalyst and without water. (a), (b) Oxidation channels. (c−e) Reduction channels. (f) Side channels. Label (a) as "CO_2 channel from ligands (minor)" and (b) as "O_2 channel (major)".

The DRIFT spectra with KBr as a reference show changes occurring in the surface capping ligand (Figure 4a), whereas by using PeNC/N_2 as a reference, the capping ligand vibrations can be excluded to identify chemical species arising due to CO_2 reduction (Figure 4b). The black spectrum in Figure 4a shows IR vibrational lines of surface-bound ligands and chemisorbed CO_2 molecules that underwent significant changes subject to irradiation. After irradiation, an isosbestic point ~3220 cm^{-1} between the rising band (i) and decaying band (ii) implies interconversion from ammonium (including both oleylammonium and formamidinium) to form bound hydroxyl, free oleylamine, and possibly a trace of water. Band (iii) represents vibrational modes of bound OA and OLA ligands that underwent decomposition upon irradiation. The vibrational lines observed in the region 1400−1600 cm^{-1} labeled as (vi) correspond to bound oleate formed due to interaction between OA and Pb.[26,27] The intensities of these lines decreased with time, indicating that bound oleate (vi) might accept a hole from PeNC and detach from the surface in the form of oleic acid radical, which might decompose to oleyl radical and CO_2, as shown in Figure 5a.[28,29] The production of CO_2 in this channel is responsible to form CO in the control experiment in the absence of CO_2 on PeNC; detachment of the oleyl radical from PeNC would leave space for CO_2 adsorption on PeNC. Another channel as oxidation path is shown in Figure 5b. The surface-bound hydroxyls,[30,31] generated from reduction channels to be discussed, can accept two holes and release a proton to form a bound oxygen cation.[30] This cation can either take a water and release a proton (not shown)[30] or directly take a hydroxyl anion (either

https://doi.org/10.1021/acsenergylett.2c02342
ACS Energy Lett. 2023, 8, 280−288

free OH− or a bound OH nearby) to form a surface-bound peroxide species;[30] it eventually takes another two holes and releases another proton to form an oxygen molecule, leaving a vacancy for the PeNC to accept CO_2 for further reduction.

For the reduction path, the formation of bound dioxycarbon anion (Pb−OCO^-) is expected as the first step to initiate CO_2 reduction; evolution of two bands, indicated with dashed lines (v), represents formation of the dioxycarbon anion[32,33] through electron transfer from PeNC to CO_2. As Figure 4b shows, band (v) at 1680 cm^{-1} begins to appear after irradiation and continues to grow for 20 min; three bands (iv) represent the formate species[34] formed after a dioxycarbon anion accepted a proton from FA or OLA cation. Based on this observation, we expect that CO and bound hydroxyls were formed via electron rearrangement according to the scheme shown in Figure 5c. Both Figure 4a,b show that three bands of (vii) arose through formation of the monodentate carbonate anion,[33] which would accept a proton (from FA or OLA) to form a bicarbonate species[32,33] indicated as two bands (viii). We hence propose a reduction channel involving formation of monodentate and bicarbonate intermediates in Figure 5d, for which bound hydroxyl, CO, and free OH^- anion formed after several electron rearrangements.

Both formate and bicarbonate channels (Figure 5c,d) produce bound hydroxyl that is a key species in Figure 5b for the oxidation channel to generate oxygen; the production of free OH^- anion in Figure 5d can supply the O_2 channel in Figure 5b. Formation of formate and bicarbonate species requires accepting additional protons, which can be supplied from either the oxygen channel (Figure 5b) or the ammonium (FA or OLA) deprotonation channel aforementioned. The intensity of line (ix), corresponding to a chelating bridge carbonate species[32,35] increased and remained constant after 60 min. We hence propose a bidentate channel to form bridge carbonate and CO in Figure 5e. The bridge carbonate might break the Pb−O bond to form monodentate carbonate and then follow the reduction path via Figure 5d to form bound hydroxyl, CO, and free OH^- anion. The side reactions including formation of oleyl dimer and water appear in Figure 5f. The formation of methane is a minor channel to be considered, which can follow the reduction of formate via formation of a methoxy intermediate reported elsewhere.[14]

For the reaction mechanism discussed in Figure 5, we consider the half reactions for the reduction and oxidation channels in eq 4 and eq 5, respectively:

$$CO_2 + H^+ + 2e^- \rightarrow CO + OH^- \qquad \text{(Figure 5c)} \tag{4}$$

$$OH^- \rightarrow \frac{1}{2}O_2 + H^+ + 2e^- \qquad \text{(Figure 5b)} \tag{5}$$

To evaluate the redox potentials for eq 4 and eq 5, we include side reaction $H_2O \rightarrow H^+ + OH^-$ in reaction 4 and $H^+ + OH^- \rightarrow H_2O$ in reaction 5 to obtain the following redox reactions,

$$CO_2 + H_2O + 2e^- \rightarrow CO + 2OH^- \qquad E^0_{red} = -0.934\ V \tag{6}$$

$$2OH^- \rightarrow \frac{1}{2}O_2 + H_2O + 2e^- \qquad E^0_{ox} = -0.401\ V \tag{7}$$

(see refs 24 and 25, respectively) for which reaction 1 can be produced via redox reactions 4 and 5 to give the overall potential −1.335 V that is the same as that required for redox reactions 2 and 3, consistent for the overall reaction 1 with a standard Gibbs energy of reaction 257.2 kJ mol^{-1}.[25] In the absence of water, OH^- in reaction 5 is a bound hydroxyl that can readily accept two holes to initiate the oxidation according to the mechanism in Figure 5b. For twice reaction 5, one OH^- is a bound hydroxyl; the other is a free OH^- produced via the reduction channel (Figure 5d). The monodentate reduction channel (Figure 5c) requires two electrons and one proton to generate one CO and one bound hydroxyl; the bidentate channels (Figure 5d,e) require four electrons and two protons to generate two CO, one bound hydroxyl, and one free OH^- according to twice reaction 4. Water oxidation, reaction 3, is a bottleneck for CO_2 reduction with water present, but in its absence the hydroxyl oxidation channel, reaction 5, has much lower potential to generate protons required for CO_2 reduction to proceed.

In conclusion, lead-halide perovskite materials are sensitive to moisture that limits their applications in a traditional photocatalytic reduction of carbon dioxide with water as hole scavenger. We here report the first example of self-photocatalytic CO_2 reduction using mixed cationic perovskite nanocrystals (PeNC), $Cs_{0.55}FA_{0.45}PbBr_3$ (CF), as an efficient photocatalyst at the gas−solid interface in the absence of water. This redox reaction generates CO and O_2 in ratio 2:1, fulfilling the stoichiometric ratio for CO_2 self-photocatalytic decomposition. The best CO yield 1.26 mmol g^{-1} and average yield 1.11 mmol g^{-1} within 12 h is three times that using $CsPbBr_3$ (CS) PeNC as a catalyst. The best rate of CO production was 105 μmol g^{-1} h^{-1}, which is more than 2.3 times that in any report at a gas−solid interface. Based on time-dependent DRIFT results for the CF catalyst, bound hydroxyl species OH^- plays an important role in the oxidation channel to generate O_2 and leaves vacancies for CO_2 to adsorb; bound dioxycarbon anion $-OCO^-$ plays a key role in the reduction channel to generate CO and both bound and free OH^- to replenish the oxidation channel. The yield of CO without water was twice that with water present. The CO_2 adsorbed on the surface of CF is reduced to CO, and the remaining oxygen atom attached on CF is oxidized to form an oxygen molecule. This is the first example of self-photocatalysis that splits CO_2 into CO and O_2 in the absence of water, with the highest yield of CO ever recorded. Our work thus provides a new concept and an efficient method for photocatalytic conversion of CO_2 to decrease greenhouse gas and hopefully to solve the important problems of global warming.

■ ASSOCIATED CONTENT

Supporting Information

The Supporting Information is available free of charge at https://pubs.acs.org/doi/10.1021/acsenergylett.2c02342.

Description of experimental details using the hot-addition method to synthesize perovskite nanocrystals, procedures of photocatalytic CO_2 reduction, supplemental Figures S1−12 and Tables S1−3 including the results of XRD, TOPAS analysis, TEM, UV−vis absorption spectra, TEM-EDX, SEM-EDX, GC-FID, GC-TCD, GC−MS, recycling product yield measurements, lattice parameters, and spectral assignments (PDF)

https://doi.org/10.1021/acsenergylett.2c02342
ACS Energy Lett. 2023, 8, 280−288

AUTHOR INFORMATION

Corresponding Authors

Sue-min Chang − *Institute of Environmental Engineering, National Yang Ming Chiao Tung University, Hsinchu 300093, Taiwan;* orcid.org/0000-0003-3548-145X; Email: chang@nycu.edu.tw

Eric Wei-Guang Diau − *Department of Applied Chemistry and Institute of Molecular Science and Center for Emergent Functional Matter Science, National Yang Ming Chiao Tung University, Hsinchu 300093, Taiwan;* orcid.org/0000-0001-6113-5679; Email: diau@nycu.edu.tw

Authors

Sumit S. Bhosale − *Department of Applied Chemistry and Institute of Molecular Science, National Yang Ming Chiao Tung University, Hsinchu 300093, Taiwan*

Aparna K. Kharade − *Institute of Environmental Engineering, National Yang Ming Chiao Tung University, Hsinchu 300093, Taiwan*

Sudhakar Narra − *Department of Applied Chemistry and Institute of Molecular Science and Center for Emergent Functional Matter Science, National Yang Ming Chiao Tung University, Hsinchu 300093, Taiwan;* orcid.org/0000-0003-4893-9204

Complete contact information is available at: https://pubs.acs.org/10.1021/acsenergylett.2c02342

Author Contributions

#S.S.B. and A.K.K. contributed equally.

Author Contributions

E.W.G.D. and S.C. conceived of this study, S.S.B., A.K.K., and S.N. designed and conducted the CO_2 reduction experiments, S.S.B. performed the TEM and XRD measurements and analysis, S.S.B. and A.K.K. performed time-dependent DRIFT measurements, E.W.G.D., S.C., and S.S.B. interpreted the data and proposed the mechanism, E.W.G.D., S.S.B., and S.N. drafted the manuscript, and all authors contributed to interpret the experimental results and to finalize the manuscript.

Notes

The authors declare no competing financial interest.

ACKNOWLEDGMENTS

The authors thank Y.-P. Lee and C.-H. Hung for valuable discussions. This work is supported by the National Science and Technology Council (NSTC), Taiwan (Grant Nos. NSTC 111-2634-F-A49-007 and NSTC 111-2123-M-A49-001) and the Centre for Emergent Functional Matter Science of National Yang Ming Chiao Tung University (NYCU) from The Featured Areas Research Centre Program within the framework of the Higher Education Sprout Project by the Ministry of Education (MOE) in Taiwan.

REFERENCES

(1) Wu, J.; Huang, Y.; Ye, W.; Li, Y. CO_2 Reduction: From the Electrochemical to Photochemical Approach. *Adv. Sci.* **2017**, *4* (11), 1700194.

(2) Li, X.; Sun, Y.; Xu, J.; Shao, Y.; Wu, J.; Xu, X.; Pan, Y.; Ju, H.; Zhu, J.; Xie, Y. Selective Visible Light Driven Photocatalytic CO_2 Reduction to CH_4 Mediated by Atomically Thin $CuIn_5S_8$ Layers. *Nat. Energy* **2019**, *4* (8), 690−699.

(3) Niu, K.; Xu, Y.; Wang, H.; Ye, R.; Xin, H. L.; Lin, F.; Tian, C.; Lum, Y.; Bustillo, K. C.; Doeff, M. M.; Koper, M. T. M.; Ager, J.; Xu, R.; Zheng, H. A Spongy Nickel Organic CO_2 Reduction Photocatalyst for Nearly 100% Selective CO Production. *Sci. Adv.* **2017**, *3* (7), 1700921.

(4) Xu, Y.-F.; Yang, M.-Z.; Chen, B.-X.; Wang, X.-D.; Chen, H.-Y.; Kuang, D.-B.; Su, C.-Y. A $CsPbBr_3$ Perovskite Quantum Dot/Graphene Oxide Composite for Photocatalytic CO_2 Reduction. *J. Am. Chem. Soc.* **2017**, *139* (16), 5660−5663.

(5) Wu, L.; Mu, Y.; Guo, X.; Zhang, W.; Zhang, Z.; Zhang, M.; Lu, T. Encapsulating Perovskite Quantum Dots in Iron-Based Metal−Organic Frameworks (MOFs) for Efficient Photocatalytic CO_2 Reduction. *Angew. Chemie Int. Ed.* **2019**, *58* (28), 9491−9495.

(6) Shyamal, S.; Pradhan, N. Halide Perovskite Nanocrystal Photocatalysts for CO_2 Reduction: Successes and Challenges. *J. Phys. Chem. Lett.* **2020**, *11* (16), 6921−6934.

(7) Xu, Y.; Zhang, W.; Su, K.; Feng, Y.; Mu, Y.; Zhang, M.; Lu, T. Glycine-Functionalized $CsPbBr_3$ Nanocrystals for Efficient Visible-Light Photocatalysis of CO_2 Reduction. *Chem. − A Eur. J.* **2021**, *27* (7), 2305−2309.

(8) Chen, Y.-H.; Ye, J.-K.; Chang, Y.-J.; Liu, T.-W.; Chuang, Y.-H.; Liu, W.-R.; Liu, S.-H.; Pu, Y.-C. Mechanisms behind Photocatalytic CO_2 Reduction by $CsPbBr_3$ Perovskite-Graphene-Based Nano-heterostructures. *Appl. Catal. B Environ.* **2021**, *284*, 119751.

(9) Xu, F.; Meng, K.; Cheng, B.; Wang, S.; Xu, J.; Yu, J. Unique S-Scheme Heterojunctions in Self-Assembled $TiO_2/CsPbBr_3$ Hybrids for CO_2 Photoreduction. *Nat. Commun.* **2020**, *11* (1), 4613.

(10) Shyamal, S.; Dutta, S. K.; Pradhan, N. Doping Iron in $CsPbBr_3$ Perovskite Nanocrystals for Efficient and Product Selective CO_2 Reduction. *J. Phys. Chem. Lett.* **2019**, *10* (24), 7965−7969.

(11) Guo, S.-H.; Zhou, J.; Zhao, X.; Sun, C.-Y.; You, S.-Q.; Wang, X.-L.; Su, Z.-M. Enhanced CO_2 Photoreduction via Tuning Halides in Perovskites. *J. Catal.* **2019**, *369*, 201−208.

(12) Sheng, J.; He, Y.; Li, J.; Yuan, C.; Huang, H.; Wang, S.; Sun, Y.; Wang, Z.; Dong, F. Identification of Halogen-Associated Active Sites on Bismuth-Based Perovskite Quantum Dots for Efficient and Selective CO_2 to CO Photoreduction. *ACS Nano* **2020**, *14* (10), 13103−13114.

(13) Raza, M. A.; Li, F.; Que, M.; Zhu, L.; Chen, X. Photocatalytic Reduction of CO_2 by Halide Perovskites: Recent Advances and Future Perspectives. *Mater. Adv.* **2021**, *2* (22), 7187−7209.

(14) Bhosale, S. S.; Kharade, A. K.; Jokar, E.; Fathi, A.; Chang, S.; Diau, E. W.-G. Mechanism of Photocatalytic CO_2 Reduction by Bismuth-Based Perovskite Nanocrystals at the Gas−Solid Interface. *J. Am. Chem. Soc.* **2019**, *141* (51), 20434−20442.

(15) Das, R.; Chakraborty, S.; Peter, S. C. Systematic Assessment of Solvent Selection in Photocatalytic CO_2 Reduction. *ACS Energy Lett.* **2021**, *6* (9), 3270−3274.

(16) San Martin, J.; Dang, N.; Raulerson, E.; Beard, M. C.; Hartenberger, J.; Yan, Y. Perovskite Photocatalytic CO_2 Reduction or Photoredox Organic Transformation? *Angew. Chemie Int. Ed.* **2022**, *61*, No. e202205572.

(17) Bhosale, S. S.; Narra, S.; Jokar, E.; Manikandan, A.; Chueh, Y.-L.; Diau, E. W.-G. Functionalized Hybrid Perovskite Nanocrystals with Organic Ligands Showing a Stable 3D/2D Core/Shell Structure for Display and Laser Applications. *J. Mater. Chem. C* **2021**, *9* (48), 17341−17348.

(18) Bhosale, S. S.; Jokar, E.; Chiang, Y.-T.; Kuan, C.-H.; Khodakarami, K.; Hosseini, Z.; Chen, F.-C.; Diau, E. W.-G. Mn-Doped Organic−Inorganic Perovskite Nanocrystals for a Flexible Luminescent Solar Concentrator. *ACS Appl. Energy Mater.* **2021**, *4* (10), 10565−10573.

(19) Protesescu, L.; Yakunin, S.; Bodnarchuk, M. I.; Krieg, F.; Caputo, R.; Hendon, C. H.; Yang, R. X.; Walsh, A.; Kovalenko, M. V. Nanocrystals of Cesium Lead Halide Perovskites ($CsPbX_3$, X = Cl, Br, and I): Novel Optoelectronic Materials Showing Bright Emission with Wide Color Gamut. *Nano Lett.* **2015**, *15* (6), 3692−3696.

(20) Cottingham, P.; Brutchey, R. L. On the Crystal Structure of Colloidally Prepared $CsPbBr_3$ Quantum Dots. *Chem. Commun.* **2016**, *52* (30), 5246−5249.

(21) He, M.; Wang, C.; Li, J.; Wu, J.; Zhang, S.; Kuo, H.-C.; Shao, L.; Zhao, S.; Zhang, J.; Kang, F.; Wei, G. $CsPbBr_3-Cs_4PbBr_6$

Composite Nanocrystals for Highly Efficient Pure Green Light Emission. *Nanoscale* **2019**, *11* (47), 22899−22906.
(22) DuBose, J. T.; Christy, A.; Chakkamalayath, J.; Kamat, P. V. Transformation of Perovskite Nanoplatelets to Large Nanostructures Driven by Solvent Polarity. *ACS Mater. Lett.* **2022**, *4* (1), 93−101.
(23) Narra, S.; Bhosale, S.; Kharade, A.; Chang, S.-M.; Diau, E. W. -G. Retarded Charge Recombination to Enhance Photocatalytic Performance for Water-Free CO_2 Reduction Using Perovskite Nanocrystals as Photocatalysts. *J. Phys. Chem. Lett.* **2022**, *13*, 9134−9139.
(24) Qiao, J.; Liu, Y.; Hong, F.; Zhang, J. A Review of Catalysts for the Electroreduction of Carbon Dioxide to Produce Low-Carbon Fuels. *Chem. Soc. Rev.* **2014**, *43* (2), 631−675.
(25) Engle, T.; Reid, P.*Physical Chemistry*, third ed.; Pearson Education Inc., 2013.
(26) Perez De Berti, I. O.; Cagnoli, M. V.; Pecchi, G.; Alessandrini, J. L.; Stewart, S. J.; Bengoa, J. F.; Marchetti, S. G. Alternative Low-Cost Approach to the Synthesis of Magnetic Iron Oxide Nanoparticles by Thermal Decomposition of Organic Precursors. *Nanotechnology* **2013**, *24* (17), 175601.
(27) Bronstein, L. M.; Huang, X.; Retrum, J.; Schmucker, A.; Pink, M.; Stein, B. D.; Dragnea, B. Influence of Iron Oleate Complex Structure on Iron Oxide Nanoparticle Formation. *Chem. Mater.* **2007**, *19* (15), 3624−3632.
(28) Buz, E.; Morlet-Savary, F.; Lalevée, J.; Acar, H. Y. CdS-Oleic Acid Quantum Dots as Long-Wavelength Photoinitiators in Organic Solvent and Preparation of Luminescent, Colloidal CdS/Polymer Nanocomposites. *Macromol. Chem. Phys.* **2018**, *219* (2), 1700356.
(29) Orrison, C.; Meeder, J. R.; Zhang, B.; Puthenpurayil, J.; Hall, M. B.; Nippe, M.; Son, D. H. Efficient Redox-Neutral Photocatalytic Formate to Carbon Monoxide Conversion Enabled by Long-Range Hot Electron Transfer from Mn-Doped Quantum Dots. *J. Am. Chem. Soc.* **2021**, *143* (27), 10292−10300.
(30) Venugopal, A.; Egberts, L. H. T.; Meeprasert, J.; Pidko, E. A.; Dam, B.; Burdyny, T.; Sinha, V.; Smith, W. A. Polymer Modification of Surface Electronic Properties of Electrocatalysts. *ACS Energy Lett.* **2022**, *7*, 1586−1593.
(31) Kreft, S.; Schoch, R.; Schneidewind, J.; Rabeah, J.; Kondratenko, E. V.; Kondratenko, V. A.; Junge, H.; Bauer, M.; Wohlrab, S.; Beller, M. Improving Selectivity and Activity of CO_2 Reduction Photocatalysts with Oxygen. *Chem.* **2019**, *5* (7), 1818−1833.
(32) Wang, M.; Shen, M.; Jin, X.; Tian, J.; Li, M.; Zhou, Y.; Zhang, L.; Li, Y.; Shi, J. Oxygen Vacancy Generation and Stabilization in CeO_{2-x} by Cu Introduction with Improved CO_2 Photocatalytic Reduction Activity. *ACS Catal.* **2019**, *9* (5), 4573−4581.
(33) Zhao, H.; Liu, L.; Andino, J. M.; Li, Y. Bicrystalline TiO_2 with Controllable Anatase−Brookite Phase Content for Enhanced CO_2 Photoreduction to Fuels. *J. Mater. Chem. A* **2013**, *1* (28), 8209.
(34) Liu, L.; Zhao, H.; Andino, J. M.; Li, Y. Photocatalytic CO_2 Reduction with H_2O on TiO_2 Nanocrystals: Comparison of Anatase, Rutile, and Brookite Polymorphs and Exploration of Surface Chemistry. *ACS Catal.* **2012**, *2* (8), 1817−1828.
(35) Du, H.; Williams, C. T.; Ebner, A. D.; Ritter, J. A. In Situ FTIR Spectroscopic Analysis of Carbonate Transformations during Adsorption and Desorption of CO_2 in K-Promoted HTlc. *Chem. Mater.* **2010**, *22* (11), 3519−3526.

https://doi.org/10.1021/acsenergylett.2c02342
ACS Energy Lett. 2023, 8, 280−288